Eur. Phys. J. Special Topics **225**, 3061–3085 (2016)

DOI: 10.1140/epjst/e2016-60018-x

THE EUROPEAN PHYSICAL JOURNAL SPECIAL TOPICS

Review

Interaction of Rydberg atoms with surfaces

Using surface ionisation as a probe for surface analysis

Mike W. Kohlhoff [a]

Department of Chemistry, University of Oxford, Chemistry Research Laboratory, Oxford OX1 3TA, UK

Received 1 February 2016 / Received in final form 15 July 2016
Published online 19 December 2016

Abstract. The interface of neutral Rydberg atoms in the gas phase with a solid surface is of interest in many fields of modern research. This interface poses a particular challenge for any application in which Rydberg atoms are close to a substrate but also opens up the possibility of studying properties of the surface material itself through the atomic response. In this review the focus is on the process of electron tunneling from the excited state into the substrate that occurs when a Rydberg atom is located in front of a surface at a range of a few hundred nm and is demonstrated with a metallic surface. It is shown how variations in this ionisation mechanism can provide a powerful tool to probe image-charge effects, measure small superficial electric stray or patch fields and how charge transfer from the Rydberg atom can be in resonance with energetically discrete surface states.

1 Rydberg atoms at surfaces and interfaces

When atoms are excited into states of high principal quantum number n their properties are exaggerated and long-range interactions lead to a strong coupling with their environment. The electron cloud is greatly expanded compared to the ground state ($\propto n^2$) which results in a large polarisability of a Rydberg state ($\propto n^7$) causing a strong response to electric fields [1]. In terms of a classical dipole, the positive core and negative electron are widely separated giving these excited states a large dipole moment, by which Rydberg atoms exhibit interactions over great distances ($\sim \mu$m), where the interactions can be controlled externally. The range of exotic properties makes them an interesting subject in various fields of research, Rydberg atoms are used in cavity quantum electrodynamics [2,3], in controlled chemical reactions by mechanical manipulation [4], serve as a model system for dipole-mediated energy transport in biological systems [5], can be used as a non-linear medium to mediate single-photon interactions [6,7] and have been proposed in several ways for quantum information processing [9–12]. However, this also means that the strong interaction will not be limited to surrounding atoms but that they also couple to condensed matter, bulk surfaces, in the vicinity. See Fig. 1 for an overview of Rydberg-surface interactions.

[a] e-mail: mike.kohlhoff@chem.ox.ac.uk

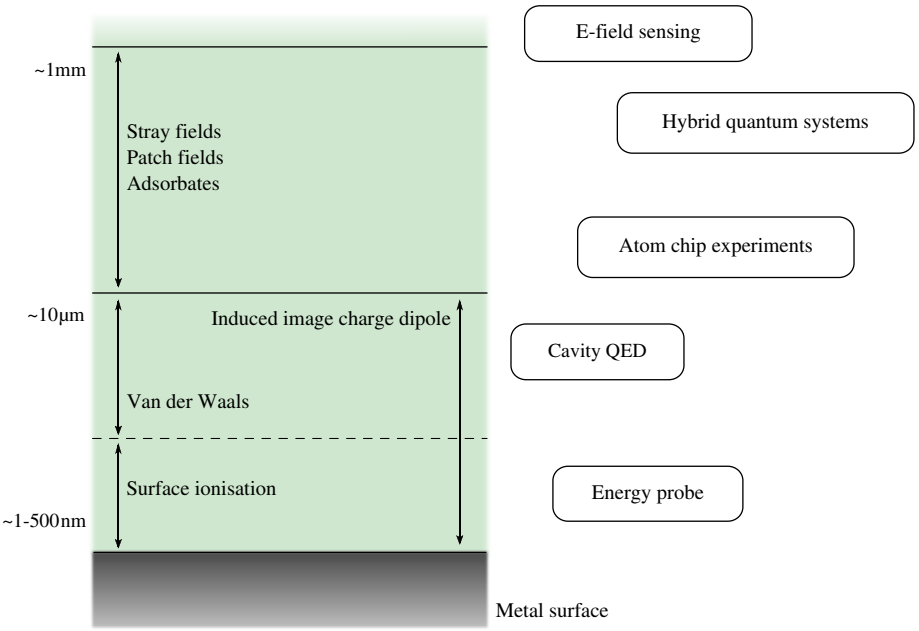

Fig. 1. Different interaction types for neutral Rydberg atoms interfaced with a metallic surface and the distance ranges spanned by these interactions. The relevance of these distance regimes for typical applications and fields of research is noted on the right side.

It has been suggested that the long range interaction of Rydberg states may be facilitated by enclosing a Rydberg gas at room temperature in wedge shaped glass cells with the attempt to implement integrable gates and single photon devices [8]. Other proposals have concentrated on combining Rydberg atoms in the gas phase with a solid-state coplanar waveguide [13] where the waveguide can hold a superconducting qubit which is a highly promising candidate for the successful large-scale implementation of quantum information [14]. This hybrid approach combines the advantages of the two different quantum system: the strong coupling of the macroscopic solid-state device and the long radiative lifetimes ($\tau \propto n^3$) of a Rydberg state of up to ms [15,16]. Here, the Rydberg atom in the hybrid system can enhance the comparatively short coherence times of the superconducting qubit of a few tens of μs [17] and also act like a memory or transmitter by transferring information from one part of the device to the other.

Even though the special characteristics of these high lying states offer a unique degree of control and manipulation, this ability comes with the price of their being easily perturbed by their environment. If the aim is to implement these ideas practically, miniaturisation will be a key factor, and closer interfacing of a Rydberg gas to metal and dielectric components of the apparatus is inevitable.

1.1 Long-range interaction with surfaces

For the aforementioned schemes to be feasible, the understanding of the interplay of Rydberg atoms with small electric fields becomes crucially important. The fields can be produced by the roughness and geometric structure of nearby surfaces, or they may originate from patch charges on them. In the context of information processing, the effect of adsorbates has been investigated by a number of groups over the last

few years. In a seminal work, Tauschinsky et al. investigated energy-level shifts above the gold-coated surface of a permanent magnetic substrate via electromagnetically induced transparency (EIT) [18]. They found the level shifts to be distance-dependent and caused by spatially inhomogeneous electric fields originating from adatoms adsorbed on the chip surface. The magnitude of these fields scales with the height as $\propto z^{-0.7}$, contrary to the fields due to randomly distributed patch potentials which scale with z^{-2} [19]. The Rubidium atoms are excited to Rydberg states and held in micron-sized traps $10\,\mu$m above a patterned magnetic film [20] and are lost from the traps over time, depositing as mounds on the substrate. Work on the adsorption of neutral atoms onto the surface of an atom chip was further complemented by Hattermann et al. who also used EIT to probe an atom cloud released from optical tweezers onto a copper surface. They were able to determine that electrostatic fields arising from the adsorbed Rubidium are about 1 V cm in magnitude and that these fields formed after a mere 100 repetitions of their experimental cycle [21].

In atom-chip experiments the detrimental effects of Rydberg-surface interaction prevent the trapping of atom clouds at distances closer than $\sim$100 nm to the substrate due to perturbation of the trapping potential [22]. In the proposal for using wedge glass cells for housing a Rydberg vapour at room temperature, the goal is to construct the spacing of the glass cells to accommodate another collective feature of a dense Rydberg sample, the Rydberg blockade. This is a mechanism in which excitation of another Rydberg state is collectively suppressed within a specific volume according to a blockade radius. To match this blockade radius, the confining compartment needs to extend several micrometres for a state in principal quantum numbers $n = 30 - 50$ [8]. The potentially significant interactions with a surface must be well understood to make, in the context of quantum information, for a maximum fidelity and a deterministic scheme that preserves atomic coherence.

In contrast to a conducting metal as a conductor, an insulator builds up a dielectric polarisation when placed in an electric field where this charging-up effect is expected to enhance the dipolar interaction of an atom with a dielectric surface, especially when adsorbates are deposited on the surface. The enlarged response to a dielectric surface can be explained by a resonant coupling to polariton and plasmon modes of the material [2,36,37]. Even though fused silica glass is a common material used in cold atom experiments it has only been studied marginally. In work by Kübler et al. and Abel et al. it was found that the shift of the Rydberg state energies deviates from the expected scaling in the presence of a dielectric that modifies the electric field response [8,38,39]. In Ref. [8] the principal quantum number of the Rydberg state is specifically chosen to minimise the coupling to polariton modes in the quartz glass. Other ways to inhibit the interaction with the substrate are to use specially designed coatings.

The extreme sensitivity to minuscule electric fields in surface architectures leads to an undesired response but this can also be used as a probe. Employing high-resolution spectroscopy of the Stark shift of Rydberg states, the magnitude of electric fields can be determined; in this way measurements of field inhomogeneities down to $\pm 20\,\mu$V have been demonstrated [23].

1.2 Short-range interaction with surfaces

Complications of using chip or hybrid designs are the energy shifts of the atomic state and altered excited state lifetimes by changes in the spontaneous emission rates [3] which are of relevance in comparatively large atom-surface separations. After the effect of stray electric fields, the next strongest coupling is interaction of a Rydberg atom with its induced image charge. The large dipole of a Rydberg state ($\propto n^2$)

induces a charge polarisation in a metallic bulk that results in an attractive net force [24]. At the smaller end of the range of separations the influence of the image-charge interactions gets more drastic, and the electron is able to pass over or tunnel through the potential barrier into the conduction band and thus is ionised [26,28].

At the closest distances to the surface, the shape of the potential landscape gains importance and it has been proposed that Rydberg atoms could be used for controlled deposition in nanolithography [25]. Surface orbitals are in general not fully occupied, which renders the surface reactive to any element or compound present in the gas phase. If the surface is exposed to a controlled environment, as when it is placed in a (ultra-) high vacuum, it becomes possible to control the exposure to potential reaction partners which makes it a model system for the study of surface chemistry.

In the following, the focus will be on the interplay of an highly excited atomic state with a metallic surface, particularly the process of ionisation, which has been a subject of several investigations over the last three decades in experimental studies [27–31] as well as in theoretical studies [32–35]. In Sect. 2 the properties of Rydberg states in external fields will be described, and then in Sect. 3 these will be compared to the properties of Rydberg states close to a solid.

2 Rydberg states in external electric fields

To understand the ionisation of a Rydberg state in front of a surface, as is addressed later, it is useful to consider the effects of a homogeneous electric field. As the electron in a Rydberg atom is distributed over a large orbital, and far removed from the core, it has a low binding energy and the atom is highly polarisable. This makes it possible to easily remove the electron from the core with modest electric fields which renders the remaining ion detectable by charged particle detectors.

2.1 The Stark effect in hydrogen

Rydberg orbitals are hydrogenic and the eigenstates at zero electric field can be described by the quantum numbers $|nml\rangle$ where n is the principal quantum number, l the orbital angular momentum quantum number, and m the magnetic quantum number referring to the projection of angular momentum onto the z axis. If a static electric field of magnitude F is applied along the z direction, a perturbing term is added to the (hydrogenic) zero-field Hamiltonian H^0; unless noted otherwise, all quantities are expressed in atomic units (a.u.).

$$H = H^0 + H^{\text{Stark}}(F) \tag{1}$$

where the Stark term can be expressed as in Eq. (2) when spherical coordinates are chosen and the z-axis is the quantization axis to describe the symmetry of the problem, with μ_z as the z-component of the dipole moment operator $\boldsymbol{\mu}$.

$$H^{\text{Stark}}(F) = -\boldsymbol{\mu}F = -\mu F_z = Fr\cos\theta. \tag{2}$$

This leads to a shift in energy that varies linearly with the applied field and thereby to a lifting of the degeneracy of the $|lm\rangle$ states. The splitting of the energy levels for a hydrogen atom is depicted in Fig. 2. In this symmetry, angular momentum l is no longer a good quantum number and the resulting wavefunctions can be described by the principal quantum number n and the magnetic quantum number m. The

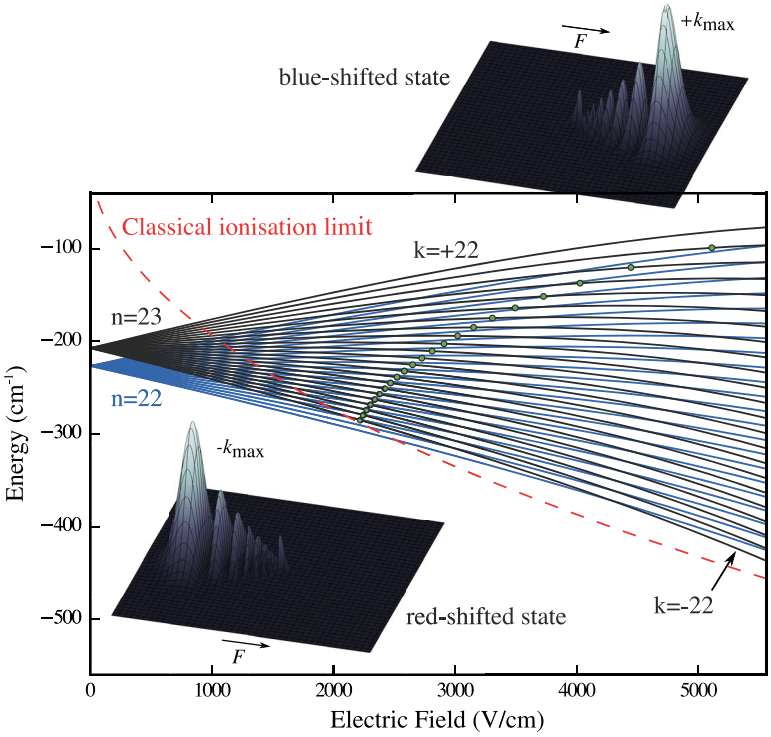

Fig. 2. Stark effect in hydrogen for $n = 23$ and $n = 22$; maximally polarised parabolic k states are labeled for $n = 23$. The crossing point of the two manifolds is the Inglis-Teller limit, beyond which no avoided crossings are observed in hydrogen. Also shown is the energy of the saddle point $V = -2\sqrt{F}$ (dashed red line) at which field ionisation is classically expected. Green circles mark field values for the different Stark states at which the ionisation rate Γ exceeds 1×10^6 s, which is the typical experimental timescale over which ionisation occurs. Note that only in the case of the most red-shifted state the classically expected field value coincides with the calculated rate. Also shown are the electron probability for polarisation parallel to the direction of the field ($+k$, blue-shifted) and in the opposite direction to the electric field ($-k$, red-shifted). The positive core is located in the middle of the plane of the wavefunction.

problem remains separable with newly-introduced parabolic quantum numbers n_1 and n_2 obeying the relation given in Eq. (3):

$$n = n_1 + n_2 + |m| + 1. \tag{3}$$

A Stark state is usually labelled by the quantum number $k = n_1 - n_2$, where k ranges from $-(n - |m| - 1)$ to $(n - |m| - 1)$ in steps of two with the total number of distinct Stark states for a given n and m being $n - |m|$.

These states have a permanent dipole moment, which manifests in a permanent polarisation along the direction of the field. A positive Stark shift corresponds to a polarisation of the electron density along the positive direction of the electric field towards higher energies (blue-shifted, $+k$) and a negative shift in the opposite direction towards lower energies (red-shifted, $-k$); exemplary probability distributions for two different maximally polarised k states are shown in Fig. 2.

Wavefunctions for extreme members of the Stark manifold in Fig. 2 illustrate that the electron distribution is highly asymmetric with the majority of the electron

probability furthest away from the core. This large separation gives the maximally polarised k states a large dipole moment ($\sim 1/2nk$) which offers a handle to exert a force on a Rydberg atom making the maximal $+k$ states an ideal candidate for spatial manipulation. An inhomogeneous field exerts a force K_{Stark} in the direction of decreasing field, or decreasing energy, with $\mathbf{K}_{\mathrm{Stark}} = -\nabla E = -\nabla(\boldsymbol{\mu}\cdot\mathbf{F})$, which allows for deceleration and deflection with small electric fields compared to a ground-state atom [41–43].

First order perturbation theory is valid for small fields that produce the linear shift of the split energies. If higher order contributions are taken into account, the energies for a specific Stark state can be calculated by the expansion in Eq. (4) [40]; the higher order effects are discernible at higher fields. For the hydrogen atom, the energies with second order corrections are

$$E^{\mathrm{Stark}}(F,n,m,k) = -\frac{1}{2n^2}+\frac{3}{2}nkF-\frac{n^4}{16}\left(17n^2-3k^2-9m+19\right)F^2+\mathcal{O}(F^3)+\ldots \quad (4)$$

Energies calculated from Eq. (4) are plotted in Fig. 2 for two different principal quantum numbers.

2.2 Ionisation in an electric field

While for modest electric fields the effect on the atom may be just an energy level shift, at higher fields ionisation can occur. This can be understood by considering the potential for the electron in the field.

If a Rydberg atom is placed in a constant electric field, the combination of the Coulomb potential (for an electron) and the linear Stark perturbation as seen by an electron has the form

$$V = -\frac{1}{r} + Fz. \quad (5)$$

This combined potential has, as depicted in Fig. 3, a saddle point on the anode side of the ion core at $z = -1/F$ with energy $V_{\mathrm{saddle}} = -2\sqrt{F}$; as the magnitude of the field increases the energy of the saddle point decreases. Classically, at a field value of $F = 16n^{-4}$ a Rydberg state would be expected to ionise as the electron can escape the Coulomb potential.

As shown in Fig. 2 it would be expected that red-shifted Stark states ionise at higher fields than blue-shifted states of the same n manifold since, at the same field value, a blue-shifted state is higher in energy. However, this is not observed experimentally. For the H atom, and for other Rydberg atoms using fast-ramped fields, blue states ionise at higher fields than red states for high principal quantum numbers n [44].

In the classical approach, the spatial extent of the electronic charge polarisation is not considered for different Stark states. In the case of a blue state, the majority of the electron density is located on the opposite side of the core to the saddle point as illustrated in Fig. 2, which makes these states kinetically more stable, leading to longer lifetimes until the ionisation event occurs. In order to achieve the same ionisation rates Γ for a blue state as for a red state, fields of higher magnitude have to be applied. A representation of the ionisation rate for different Stark states is shown in Fig. 2; the rates were calculated with a semi-empirical formula for Γ as used by Damburg and Kolosov [45].

The field-ionisation behaviour may be derived for a hydrogen atom; in the case of a nonhydrogenic species, a different behaviour is observed. For an electron in a low orbital momentum state l, which classically has a strongly elliptic orbit, the inner

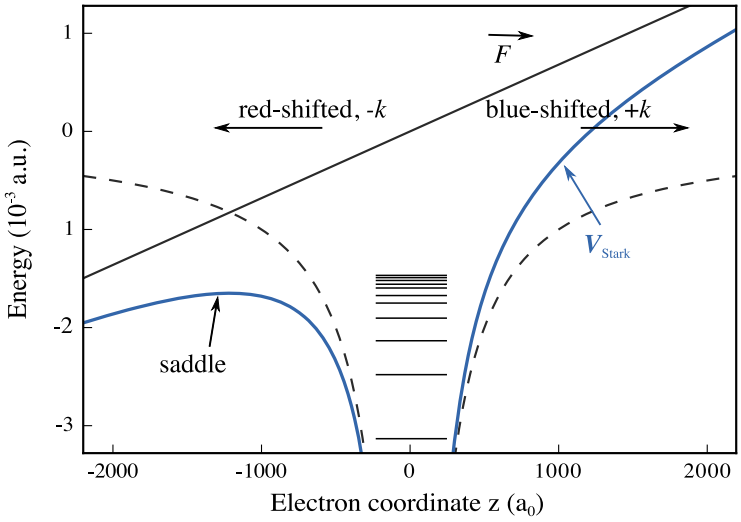

Fig. 3. Combined Stark potential (full blue line) of the perturbed Coulomb potential (dashed line), with a saddle point forming in the negative direction of the electric field. Arrows mark the direction relative to the core in which the red- and blue-shifted wavefunctions are polarised. Compare the maximally polarised wavefunctions as depicted in Fig. 2 in respect to the position of the ion core. Complementing the classical intuition, schematic energy levels are added to the plot.

part of the wavefunction is highly penetrating, causing the shielding of the core to be reduced and thereby a deviation from the Coulomb potential. The difference in energy to the hydrogen Rydberg formula is expressed through an effective quantum number $n^* = n - \delta_l$, where δ_l is the l dependent quantum defect which is 0 for hydrogen. With the Rydberg constant R_∞ the energy levels of the Rydberg series are then determined as

$$E = -\frac{R_\infty}{(n-\delta_l)^2}. \tag{6}$$

Thus, for other species, such as alkali atoms or molecules, the spherical symmetry is broken which allows coupling between red and blue states resulting in avoided crossings beyond the field value where neighbouring n manifolds cross, the Inglis-Teller limit. The field ionisation behaviour may be 'adiabatic' or 'diabatic' (hydrogen like) according to how rapidly the field is ramped up, and hence whether the system passes adiabatically or diabatically through the level crossings [26].

3 Ionisation of a Rydberg state at a metallic surface

As remarked in Sect. 1, at a distance of about 1–10 μm from the surface, the dominant net-attractive dipole interaction of Rydberg state and the surface can be described by the classical method of electrical images if the orbital size for a given n is smaller than the distance to the surface. The conduction band electrons are assumed to be mobile within the metal surface so that the material can be treated as being perfectly polarisable. Then, when an atom is brought adiabatically from an infinite distance to a large finite distance in front of the conductor, the effect can be compared to the interaction with the electrical mirror image of opposite charge at same distance beyond the surface boundary image plane [24].

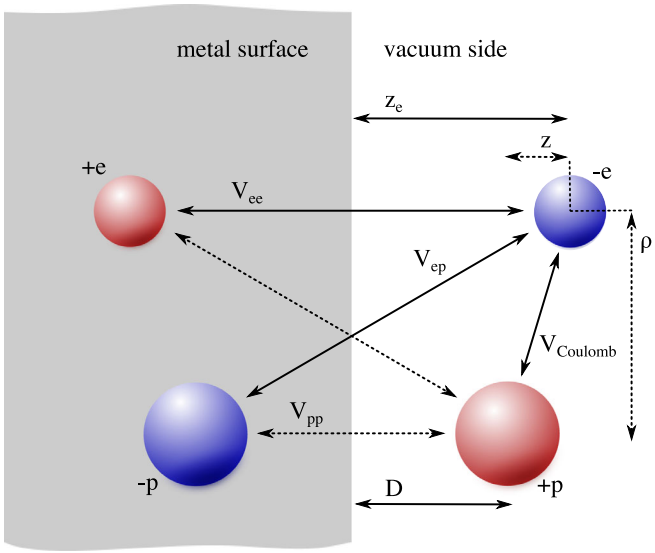

Fig. 4. Image-charge model for an atom in front of a metallic surface. The dipole on the vacuum side of the interface system induces a mirrored charge distribution in the metal that can be described by point charges. Different potential terms are labelled according to Eq. (7). The real electron is described in cylindrical symmetry by (z, ρ). The shape of the various potential contributions are further elaborated in Fig. 5.

3.1 Image-charge modelling

The contribution of the point-charge potentials for electron, ion core and their images can be isolated as depicted in Fig. 4. Choosing the surface normal as the symmetry axis, the position of the electron can then be described by (z, ρ) relative to the ion core at height D above the image plane. The total one-electron potential is then a sum of the Coulomb potential and a surface potential that is comprised of an interaction between electron and image-electron V_{ee}, an interaction V_{ep} between electron and image-proton as well as a term V_{pp} describing the interaction of proton and image-proton.

In the asymptotic long-range limit, for a charge of $q_p = e = 1$ and with $z_e = z + D$, the surface potential as the sum of the respective V_{ii} components for the Rydberg electron becomes

$$\begin{aligned} \lim_{D,\, z_e \to \infty} V_{\text{surface}} &= \lim_{D,\, z_e \to \infty} (V_{ee} + V_{pp} + V_{ep}) \\ &= -\frac{1}{4z_e} - \frac{1}{4D} + \frac{1}{\sqrt{(2D+z)^2 + \rho^2}} \end{aligned} \tag{7}$$

where the attractive V_{pp} term is cancelled by a repulsive term from the expansion but could otherwise be motivated to be omitted because it raises the energy of both the Rydberg state and the energy states of the surface equally and therefore does not affect the surface ionisation dynamics [35]. The total potential would additionally contain the Coulomb potential, $V_{\text{tot}} = V_{\text{surface}} + V_{\text{Coulomb}}$, where $V_{\text{Coulomb}} = -1/r$ and the distance r is the separation between ion core and electron.

To avoid handling the square root denominators, the components of the surface potential can be treated with a binomial expansion [46] given by:

$$V = \overbrace{-\frac{1}{r} - \frac{1}{16D^3}\left(\rho^2 + 2z^2\right)}^{D^2 \gg r^2} \underbrace{+\frac{3}{32D^4}\left(zr^2 + z^3\right) + \ldots}_{D^2 \not\gg r^2} \tag{8}$$

This potential can be used in the Hamiltonian for calculating the energy levels of the system quantum mechanically; Ganesan and Taylor included terms up to 8^{th} order to achieve convergence in their quantum calculations of the energy levels for a $n = 20$ Rydberg state.

If the atom is much further away from the surface than its orbital size, the quadratic terms are sufficient, which gives the instantaneous D^{-3} dependent van der Waals potential [47]. However, the size of a Rydberg atom grows as n^2 and the assumption that $D^2 \gg r^2$ loses its validity and Eq. (8) needs to include higher order terms in the expansion.

The van der Waals contribution introduces a perturbation that couples the hydrogenic spherical basis functions $|nlm\rangle$ with $\Delta l = 0, \pm 2$ and $\Delta m = 0$, similar to the Stark effect described above; this lifts the lm degeneracy and causes a strong polarisation of the electronic wavefunctions. A series of differently polarised states is formed where a red-shifted state is oriented towards the surface whereas a blue-shifted state is oriented towards the vacuum side of the interface system in the absence of an external field.

3.2 Surface potential modelling

As Eq. (7) is only valid for the asymptotic limit, it is unsuitable for small distances or large atom sizes since it exhibits a singularity for V_{ee} at $z = -D$, i.e. at the surface boundary. To alleviate these shortcomings, a free-electron Jellium potential as proposed by Jones et al. [48,49] can be introduced which treats the electrons as moving within a background of (positive) charge density of the ion cores in the metal. The potential is then given as

$$V_{ee}(z, D) = \begin{cases} \frac{-1+\exp(-\lambda(z_e - z_0))}{4(z_e - z_0)} & \text{if } z_e > z_0 \\ \frac{V_0}{A\exp(B(z_e - z_0))+1} & \text{otherwise} \end{cases} \tag{9}$$

$$\text{with } A = -1 - 4V_0/\lambda,\ B = -2V_0/A.$$

A and B are chosen to match V_{ee} and its derivative at the image plane position z_0. This barrier model has three further parameters to create a continuous transition from the vacuum to the bulk; λ determines the width at which the modelled potential is saturating towards U_0 where U_0 is the inner potential of the metal related to the work function of the material. The resulting Jellium surface potential system and its components are depicted in Fig. 5; it can be seen that a barrier with a saddle point is formed towards the surface.

3.3 Surface induced ionisation

This effect of the saddle point is similar to the behaviour for ionisation in an electric field, in that the saddle is lowered and decreased in width when the surface is

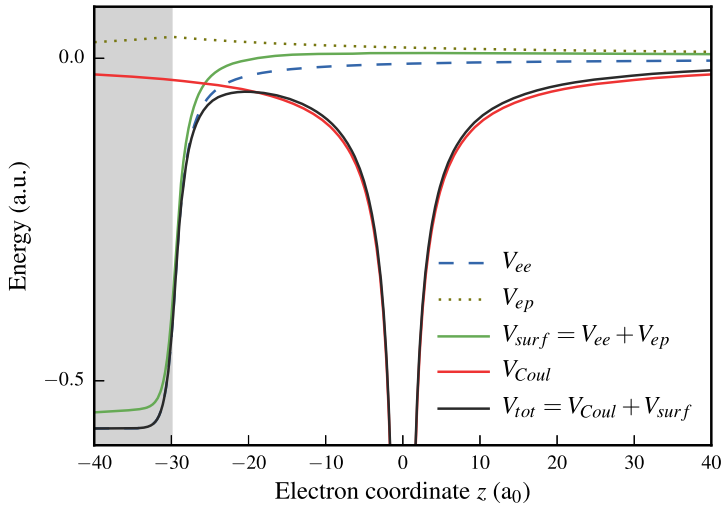

Fig. 5. Perturbation of the atomic potential induced by the presence of a surface. As explained in the text, the Jellium model for V_{ee} ensures a smooth transition of the potentials when crossing the vacuum surface boundary. The surface sits at a position of $-30\,a_0$ relative to the center of the electronic potential at $z = 0$. Note that this reference system is chosen in various calculations discussed in the text as performed by So et al. [35]. Here, the symmetry center of the atom is selected to lie statically at $z = 0$ and the surface is moved towards the atom. The parameters for the Jellium model are selected for aluminium. The figure is adapted with permission from reference [35], copyrighted by the American Physical Society.

approached by the atom. The position of the saddle point in the frame of the ion core is given in [50] as $z_s(D) \approx -0.69D$ and the height as $E_s(D) \approx 1.74/D$. Here, the perturbation of the Coulomb potential of the atom is increased as the distance between the atom and surface gets smaller as shown in Fig. 6. Analogous to the effect of a homogeneous field, the originally bound electron can escape over the potential barrier or tunnel through it into the conduction band of the metal.

When comparing the energy of the saddle point with the energy of a Rydberg state, as given in Eq. (4), the ionisation distance for the classical over-the-barrier model (OTB) can be derived in terms of n as $D_{\mathrm{OTB}} \approx 3.48n^2a_0$ [51]. For a Rydberg atom in a state $n = 30$ this predicts an ionisation distance of about 165 nm. The usefulness of the OTB model has been shown by Burgörfer et al. to characterise the reverse case, the neutralisation of an ion by charge transfer from the surface to an impinging ion [51].

This classical approach delivers a useful intuition and a good first approximation for the process of charge transfer into the metal, but cannot fully account for the actual complexity of the composite system. For example, the dynamics of resonant tunneling through the barrier are not explicitly accounted for. In the OTB approach the probability for ionisation steps from zero to one at a critical atom-surface separation whereas this step will have a finite width when the process is considered as tunneling through a barrier into a vacant level in the metal. As the surface is approached and the potential barrier decreased in width the ionisation probability increases exponentially. On the other hand, the height and width of the potential barrier displayed in Fig. 5 are not dependent on an external field, albeit such a field is usually present experimentally as discussed later.

The model also assumes that for every energy of the Rydberg state there will be an empty level in the conduction band of the metal at the same energy for transfer,

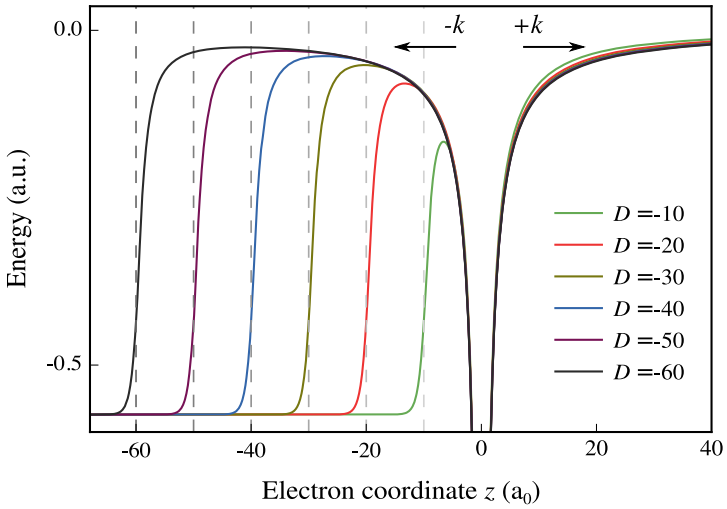

Fig. 6. Total potentials for the combined system of atom and surface with decreasing separation, which causes the saddle point that is formed towards the surface, to decrease in height and width until the electron can escape the Coulomb potential into the metal. Akin to the polarisation of the wavefunctions in an homogeneous field, a polarisation will occur either towards the surface $(-k)$ or towards the vacuum side $(+k)$.

however the model will not be appropriate if surfaces other than free-electron metals are of interest.

Importantly though, the reduced geometry of the OTB model to one dimension ($\rho = 0$) does not account for spatial effects, like polarisation of the Rydberg wavefunctions by the surface perturbation or the treatment of more complex species like molecules or nonhydrogenic atoms. Akin to the homogeneous field case, the lm degeneracy is lifted by the perturbation of the surface resulting in the formation of surface Stark states. Here, the quantisation axis is the surface normal, with states lower in energy that are oriented towards the surface $(-k)$ and higher-energy states that are oriented towards the vacuum side $(+k)$. However, the surface-perturbed energy levels within a n manifold can undergo many level crossings as the surface is approached. This has been shown by So et al. by calculating energy levels of a Rydberg state in front of a surface using a complex scaling method [35], where the crossings are attributed to breaking of parity in the z direction. Complex scaling is a coordinate transformation method used as a tool to study resonance and ionisation processes for weakly bound states. Results of such a calculation and how the energy levels cross are shown in Fig. 7.

4 Experimental studies of Rydberg charge transfer at a metal surface

In order to investigate the short range perturbation of a surface on an atom, the standard technique is to use atoms travelling in a beam directed at a surface of interest, which allows the atoms to be brought very close to the target by choosing a suitable experimental geometry.

Rydberg charge transfer has been experimentally observed with metals and with intrinsic and doped semiconductor surfaces. For the latter case, Dunham et al. found that the surface ionisation behaviour of a Si(100) sample is similar to a Au(111)

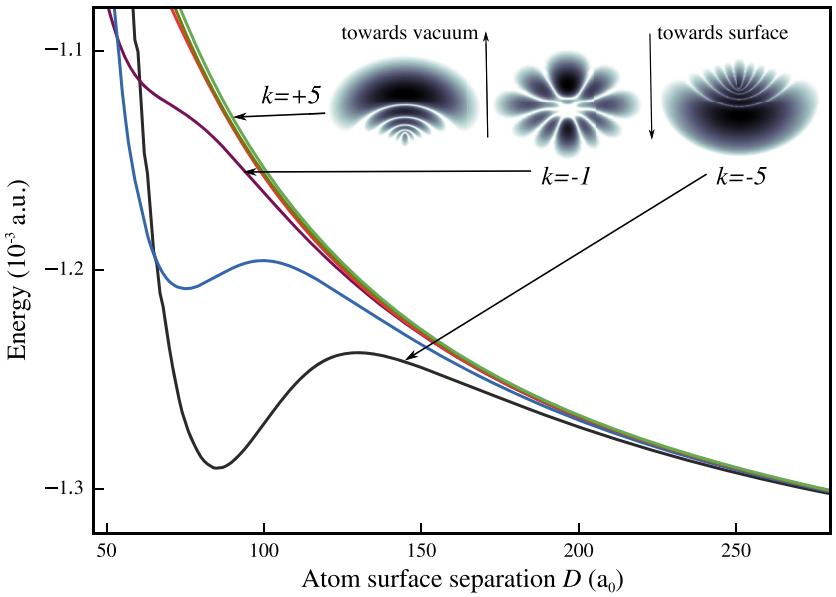

Fig. 7. Energies of hydrogen in $n = 6$, $m = 0$ as a function of distance between the atom and the surface, calculated from a complex scaling method with no extraction field present. In contrast to the homogeneous field Stark splitting, energy levels cross as the distance to the surface is reduced. But similarly, the wavefunctions are polarised, with the electron density directed either towards the surface ($-k$) or towards the vacuum ($+k$) as in the examples shown on the top. The wavefunctions are calculated with a grid based Coulomb-wave discrete variable representation (CWDVR) method.

sample [53] while Sashikesh et al. investigated the ionisation of hydrogen molecules at a silicon surface, observing different sensitivities to surface charge distributions caused by different dopant densities of either p-type or n-type silicon semiconductors [54,55]. In the context of this review, the emphasis is on the transfer of an electron from a Rydberg orbital to the conduction band of a metal.

4.1 Beam transmission through metallic grids

The earliest study of Rydberg ionisation at a solid surface was conducted by Fabre et al. [27] where sodium atoms in a beam were excited to a Rydberg state and directed at a gold foil with micrometre sized slits. The measured transmission through the slits displayed a cutoff at $n \sim 65$ at which the orbital diameter is about 100 times smaller than the slits. Evidently, the transmission is not just reduced by collision of Rydberg atoms with the gold sieve as if the atoms are assumed to behave like hard spheres; the loss of transmission is attributed to ionisation into the sieve.

Kocher and Taylor also measured the transmission of lithium Rydberg atoms through a gold mesh and over time observed a decreased survival probability. They attributed the reduced transmission to the formation of an adlayer onto the mesh material, which was formed from water molecules and lithium adsorbed on the mesh. The adlayer can form surface dipoles that are able to produce local electric fields exceeding the field ionisation threshold for a Rydberg state and atoms are thereby lost to detection since they do not pass through the mesh. The Rydberg atom experiment proved to be sufficiently sensitive to probe the orientation of these submonolayer

adsorbates alongside density variations that correspond to a surface coverage ranging from 10^{-4} to 10^{-5} monolayers [56].

In both of the aforementioned experiments the event of ionisation was inferred indirectly from the detection of Rydberg atoms travelling close to a substrate at a constant distance. In order to get access to distances near $D = 0$ in a controlled manner an atom beam can still be used, but directed at the surface at an angle. At a shallow angle this enables access of the atom beam to the surface target from the side, while leaving space in front of the target for the extraction of ions produced in the process. At the same time, this approach reduces the perpendicular component of the kinetic energy of the Rydberg atom projectile.

4.2 Ionisation in grazing incidence beams

The first experiment to directly observe the ionisation of Rydberg atoms at a solid surface was performed by Gray et al. Here, a beam of (nd) potassium atoms was excited to principal quantum numbers 17 to 30 and directed at a plane gold mirror at an angle of 2°. The Rydberg atoms that are ionised are detected by using a fine-mesh electrode located 2 mm above and parallel to the surface that creates a homogeneous electric field to accelerate ions away from the surface, and direct them at a position-sensitive detector with the aid of further extraction electrodes. In the absence of such a field the ions would travel further towards the surface and be neutralised via Auger neutralisation [57] and would not be available for detection. In that Auger process, an electron from the conduction band of the metal is transferred at close range to the ground state of the ion in the gas phase and, by energy conversation, also emitting a secondary electron into the vacuum.

The applied electric field must counteract the momentum of the ion after the ionisation event occurs and the attraction of the ion by its own image charge to the surface or the ion will collide with the surface; the higher the velocity of the ion, or the further away it is at the point of formation, the higher the magnitude of the extraction field needs to be to reverse the ion trajectory. As shown below, the minimum extraction field at which ions are observed can be translated into a distance of the ion from the surface at its point of formation and thereby the position of the Rydberg atom immediately before the event of ionisation. In this experiment the ion signal is measured over a range of extraction fields up to the value required for field ionisation, as shown in Fig. 8(b); the information about surface ionisation is then extracted from the magnitude and shape of the surface ionisation profiles (SIP). In an alternative configuration, it is also possible to extract the electrons that are formed during surface ionisation [58]. McCormack et al. demonstrated the experimental detection of an electron signal that was proposed to be the result of 'backscattered' electrons ejected away from the surface during the process of surface ionisation [35].

Assuming a perfect conductor, the field necessary to pull an ion away from its own image charge can be calculated. By considering the perpendicular components of kinetic and potential energy of the mirror system, a point charge at a distance D and with charge Z_i (= 1 for a proton) requires a minimum extraction field of

$$F_{\min}(D, T_\perp) = Z_i \left(\frac{1}{2D} + \sqrt{\frac{T_\perp}{D}} \right)^2 \tag{10}$$

where the perpendicular component of the kinetic energy of the projectile is given by $T_\perp = 1/2 m v_\perp^2$. This can be rearranged into Eq. (11) to give the minimum distance

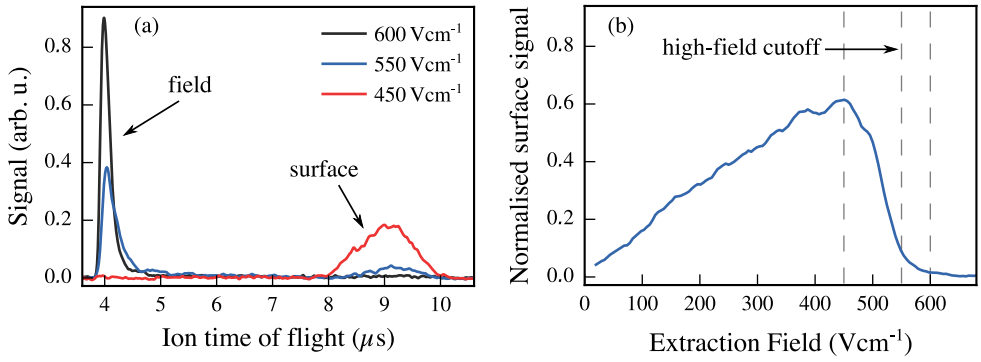

Fig. 8. (a) Typical time of flight (TOF) traces for ions produced in the process of field and surface ionisation for $n = 35$, $k = 0$. If the extraction field is lowered below the value necessary to field ionise a Rydberg atom, the onset of surface ionisation in the TOF can be observed. With the earlier field signal in the TOF than the surface signal, the flight time of the Rydberg atom towards the surface, with an extraction field present, can be deduced. (b) The gated and integrated surface signal from the TOF trace in (a); the maximum field value to extract ions from surface ionisation is marked as the high-field cutoff.

from which a positive ion can be extracted with a given field.

$$D_{\min}(F, T_\perp) = \frac{T_\perp + \sqrt{F} + \sqrt{T_\perp^2 + 2T_\perp\sqrt{F}}}{2F}. \tag{11}$$

If no field is present, the time from the event of ionisation and the subsequent acceleration of the remaining ion into the surface is very short (∼1 ns) whereas modern high voltage pulsed electronics typically have a rise time of multiple ns, hence the electric field needs to be permanently present during the process of surface ionisation. The field might have effects on the surface itself and the process of surface ionisation that are not accounted for; the effects of a surface bias field are discussed in [35].

As $T_\perp \to 0$ and incorporating the distance dependence from the OTB model, $D \propto n^2$, in the asymptotic limit of Eq. (10) the minimum detection field for hydrogen becomes

$$\lim_{T_\perp \to 0} F_{\min}(D, T_\perp) = \frac{1}{4D^2} \propto n^{-4}.$$

Thereby, Gray et al. were able to infer a distance to the target for surface ionisation and to predict a field at which appreciable ion detection should occur. In the recorded traces Gray et al. observe a discernible magnitude of ion surface signal at drastically lower fields than predicted but also a significant rise in signal at the field ranges corresponding to $\sim (4-5)n^2 a_0$; the overall shape of the ionisation traces are in stark contrast to what would be expected theoretically.

In the experimental configuration, it is inevitable that (non excited) potassium atoms travelling in the beam will be deposited on the substrate even remaining after routinely baking the surface regularly above the melting point; the deposition is minimised by collimating the beam before and after laser excitation. The difficulty arising from this is the possible neutralisation of potassium ions in the presence of an electrostatic field by collective interaction with adsorbed potassium atoms [59] since these adsorbates can locally generate high fields. The sharp onset at low extraction fields, which is independent of n, was attributed to this neutralisation process.

Despite the difficulty to predict the influences of stray fields in the previously described experiment, the results are reported with high reproducibility. In order to circumvent the adsorption of the atoms that are intended to be excited into a Rydberg state, elements can be chosen that are either less likely to react with the surface or less likely to deposit as irregular mounds of adsorbate; an obvious choice are rare-gas elements. In their subsequent experiments, Dunning and coworkers switched to the use of xenon in surface ionisation experiments with a Au(111) gold surface [30,60–62].

Under these stable and well-defined conditions Hill et al. excited xenon atoms contained in a supersonic expansion to the lowest (red-shifted) state for $13 \leq n \leq 20$ and directed the beam at a gold target at an angle of $\sim 4°$. They recorded highly efficient surface ionisation over a range of extraction voltages and found, as before, a gradual rather than a sudden rise in ionisation as the extraction field increased. The scaling of the distances for the onset of ionisation is determined as n^2, which possibly matches intuition since this is approximately the scaling of the atomic radius with principal quantum number. The distance over which ionisation occurs was derived from the experiment to be $D = (4.5 \pm 0.9)n^2 a_0$, which is in agreement with a predicted value of $\sim 3.8n^2 a_0$ from complex scaling theory that examines the broadening of Rydberg levels in the presence of a surface and bias fields [63].

Since the removal of possible large scale contamination of the surface sample can be eliminated from this version of the experiment, other reasons have to be considered as to why the surface signal still follows a shallow rise rather than a step-like trend. Hill et al. discussed the influence of the velocity distribution of the incoming atoms as well as mixing of neighbouring Stark states to partly account for the observed trace shapes. The surface preparation was further considered by comparing the surface geometries of a gold target prepared by epitaxial growth, which is near to atomically flat, to a rough machined copper surface. The latter target shows an earlier onset of surface ionisation pointing again at the importance of the shape of surface potentials.

To elucidate the influence of state changes as the surface is approached by a Rydberg atom, Dunning et al. initially prepared xenon atoms in the most red-shifted and most blue-shifted state before interacting with the surface sample [33]. The surface-ionisation profile shapes for originally red-shifted and blue-shifted states show no significant differences and the original polarisation during preparation in a static electric field is barely discernible after ion collection. These authors argued that the minimum field applied for ion detection $F_{\min}$ is mixing states of neighbouring n manifolds and by surface perturbation the approaching Stark states lose their initial identity. In contrast to hydrogen, this is due to wholly or partially adiabatic traversal of crossings in the Stark energy map as the electric field magnitude is increased; avoided crossings lead to a loss of the initial polarisation of Stark states.

Based on these findings, which cannot explain the broad shape of the ion collection signal, Wethekam et al. then focussed on investigating the ionisation rates for the lowest state in the $n = 17$ and $n = 20$ manifolds [60]. In this study it was shown that the experimental traces can be fit by modelling the ionisation expressed by a tunneling rate Γ into the metal, and by the manner in which the ionisation rate varies when the distance to the surface is decreased. First, the fraction I of incident atoms in an extraction field F with a known perpendicular component of the velocity distribution $f(v_\perp)$ that survive up to a critical distance D_c can be calculated as

$$I(F) = 1 - \int_0^\infty f(v_\perp) \times \exp\left(- \int_{D_c(F,v_\perp)}^\infty \frac{\Gamma(D', F)}{|v_\perp|} \, \mathrm{d}D' \right) \mathrm{d}v_\perp. \tag{12}$$

Tests by Wethekam et al. showed that the broad onset in the ionisation traces could not be accounted for when incorporating an experimental velocity distribution. Since

the velocity distribution does not fully explain the broadness of the ionisation onset, an ionisation rate Γ is modelled which increases exponentially with decreasing distance D'; thereby it is possible to fit the data for the most red-shifted states with

$$\Gamma(D', F) = \Gamma_0 \exp\left(-\frac{D'(1 - kF_0)}{D_{\text{decay}}}\right) \tag{13}$$

where $F_0 = n^4 F$ is the classically scaled ion extraction field, Γ_0, k and D_{decay} are constants to describe the decay of Rydberg population by ionisation. Note that the chosen characteristic decay length $D_{\text{decay}} \sim 230\, a_0$ is much larger than the expected $\sim 30\, a_0$ from hydrogenic theory.

4.3 Stray field influences on surface ionisation

While the previous model delivers a good fit to the experimental shape of the ionisation traces, it does not clarify explicitly what the reasons for this behaviour are. The potential influence of stray fields on the ionisation dynamics has been indicated several times before but not quantitatively assessed. Even though the Au(111) sample is atomically flat, it nonetheless might contain contaminants that can be a source for field inhomogeneities where any stray or patch field generated from these irregularities can reach far into the vacuum.

An approach to further investigate the effect of fields emanating from the surface is to vary the collisional angle of the incident atom beam. Considering the surface potential landscape to be (regularly) modulated by its geometric structure or surface irregularities leads to a range of effective incident angles, where the incident atom trajectories are effectively exposed to lower fields (shallower angle) and higher fields (greater angle). Varying the angle, and thereby the exposure to different parts of the surface potential, can have an impact on the onset and the shape of rising surface ionisation.

With the same apparatus as described in reference [61] Neufeld et al. investigated stray fields associated with surface inhomogeneities by varying the angle of the atom beam between $\sim 5-16$ degrees. They observed that the distance at which surface ionisation occurs is dramatically increased with increasing collisional angle, which is also expressed in large, and unphysical, decay lengths D_{decay} in the modelled ionisation rate in Eq. (13) that are mitigated by the effects of the inhomogeneities. The potential variations across the surface were modelled by the assumption of a simple periodic variation since the actual potential landscape of the gold surface is not known.

To conceptually grasp the magnitude of modulation and different domains of the surface potential Pu et al. measured the surface potentials directly via Kelvin probe force microscopy [62]. When using the measured patch fields in trajectory simulations they are able to reproduce surface ionisation for xenon with high accuracy when using a simple over-the-barrier model. Eventually, Pu et al. used an array of patterned electrodes to create a highly regular surface potential that would emulate a perfectly flat and homogeneous sample. The bias of these regularly spaced electrodes was chosen to be higher than that generated by a real surface patch so that these fields dominate the atom surface interaction rather than the actual surface potentials of the electrode array. When a modest (positive) bias is applied to the electrodes the ion signal is significantly larger at lower extraction field, implying that direct field ionisation can be achieved with stray fields originating from a structured solid sample paving the way to surface detection of low n Rydberg atoms.

4.4 Surface ionisation of molecules – further complexity

As hinted at in Sect. 3.3 the symmetry of the (classical) modelling for surface ionisation does not account for more complex species like molecules. A series of experiments studying the ionisation of hydrogen molecules at evaporated gold and aluminium surfaces was performed by Softley and coworkers [29,58,65,66]. Whereas for xenon the non-vanishing quantum defect creates a deviation from the hydrogenic behaviour, for molecules rotational (quantum number N^+) and vibrational (quantum number v^+) degrees of freedom for the core are further introduced to the problem and these might add to the dynamics of surface induced ionisation.

The first ionisation of hydrogen molecules at a surface was observed by Lloyd et al. with molecules excited to a Rydberg state with a core rotational state of $N^+ = 2$. They found that the ionisation distance scales with the size of the Rydberg orbital, as in the case of xenon ($\propto n^2$), but that the distance scaling varies with an effectively higher quantum number ν_0 that is calculated with respect to the ionisation threshold of the $N^+ = 0$ state [29]. With this effective quantum number, the distance range for surface ionisation could be determined as $D \sim (3-5)\nu_0^2 a_0^2$ which is in agreement with the results for xenon atoms.

Here, the detected onset of ionisation is more characteristic of the $N^+ = 0$ states that have a higher principal quantum number and are close in energy, hinting towards a state transition in the process. While rotational states N^+ are generally not coupled to each other in a homogeneous electric field, field inhomogeneities or perturbations by the surface image-charge interaction can introduce a coupling and facilitate a population transfer between two states of different rotational quantum numbers. In consecutive studies it was confirmed that the surface is inducing a coupling between different rotational channels of the form $|N^+ = 2, n\rangle \rightarrow |N^+ = 0, n'\rangle$, where $n' > n$, leading to a forced rotational autoionisation such that the rotational energy of the core is transferred to the Rydberg electron [65,66].

Furthermore, it was found that the observed surface ionisation does not differ with the surface material, either gold or aluminium, but shows differences towards the roughness of the material; a machined instead of evaporated aluminium exhibits a marked change in the ionisation behaviour. In the latter case the size of surface structures was ∼230 nm and thereby comparable to the size of the Rydberg orbitals.

5 Hydrogen Rydberg atoms as surface probes

In order to alleviate ambiguities in the experimental assessment of surface ionisation that are due to the adiabatic energy level crossings in the excited species as described in the previous section, the use of atomic hydrogen is an evident but challenging choice. Theoretically, it allows the direct comparison of the results from *ab initio* calculations to the experimental outcome. With other species, the nonhydrogenic effects had to be estimated to account for uncertainties in experimental observations [30,60]. As explained in Sect. 2.1 hydrogen has the advantage of traversing the Stark map without undergoing avoided crossing beyond the Inglis-Teller limit. The difficulty, however, of exciting atomic hydrogen into a Rydberg state compared to an alkali metal is the large energy difference of the $1s \rightarrow 2p$ transition (Lyman alpha line L_α) which lies in the vacuum ultraviolet part of the electromagnetic spectrum and is easily absorbed in ambient air. So et al. investigated the charge transfer from hydrogen atoms to a gold surface for the first time [31].

5.1 Experimental apparatus to study surface ionisation

In the hydrogen Rydberg atom surface experiment, H atoms are produced by photodissociation of a supersonic beam of ammonia. In a supersonic expansion, or molecular beam, a high pressure reservoir equipped with a small orifice (valve) is briefly opened ($\sim$10 μs) towards a high vacuum chamber. When the high pressure gas passes through the valve the molecules will frequently undergo collisions which results in an adiabatic cooling of the expanded gas which is distributed around a mean velocity [67]. This velocity distribution is characterised by a temperature of less than 1 K while the lab-frame velocity is controlled by seeding in a rare gas.

The expansion is released into a quartz capillary that is mounted in front of a pulsed valve [68] at the focus of a ArF excimer laser operating at 193 nm which dissociates ammonia to produce hydrogen. After the expansion which cools the H atoms to the carrier gas temperature the beam passes through a skimmer mounted between two differentially pumped chambers and travels for about 0.5 m towards the interaction region.

Rydberg excitation is achieved with two counter propagating (pulsed) lasers using a two-photon resonant transition via the $2p$ intermediate state to Rydberg states in the range $n = 20$ to 40. The two lasers are frequency doubled dye lasers that are pumped by a Nd:YAG laser where the second photon (UV) of the transition ranges from 365–379 nm. The vacuum ultraviolet light (VUV) is produced by focussing one laser beam into a mixture of krypton and argon. This rare gas mixture enables third harmonic generation to produce the L_α photon at 121.6 nm that is collimated into the interaction region with a lithium fluoride lens. The time delay between the photodissociation and the Rydberg excitation can be adjusted which allows selection of different parts of the velocity distribution. The long path between the capillary and the interaction region and the width of respective laser pulses $<$10 ns gives a velocity resolution of $\sigma \sim 1\%$. An overview of the experimental apparatus is shown in Fig. 9.

The molecular beam is directed at the surface at an angle of 20° and the counter propagating beams cross the hydrogen beam about 2–3 mm in front of the target. Ions are extracted by a mesh electrode that is parallel to the surface at a distance of about 1 cm, followed by a stack of electrodes to direct the collected ions towards a multichannel plate and phosphor-screen detector. The field and surface ionisation signals are separated in time by integrating TOF traces like the example shown in Fig. 8 over the different arrival times. The extraction field is scanned from 0 to above the onset of field ionisation and the magnitude of the gated and integrated field ionisation signal is used to normalise the surface signal.

5.2 Surface induced wavefunction polarisation in hydrogen

So et al. used this apparatus to record surface ionisation profiles (signal versus extraction field) for hydrogen in selected Stark states for a range of principal quantum numbers; by applying a small bias voltage to the surface a specific state can be selected spectroscopically from the Stark manifold. The bias field ($\ll F_{\text{extraction}}$) is present during Rydberg excitation and chosen so that the initial orientation of the electron polarisation matches the wavefunction polarisation due to the surface perturbation, as illustrated in Fig. 7, i.e. a red-shifted state is oriented towards the surface and a blue-shifted state is oriented away from the surface along the surface normal.

Similar to the surface ionisation traces for xenon, a shallow rise in signal with a low-field onset can be observed as well as as a high-field cutoff, as can be seen

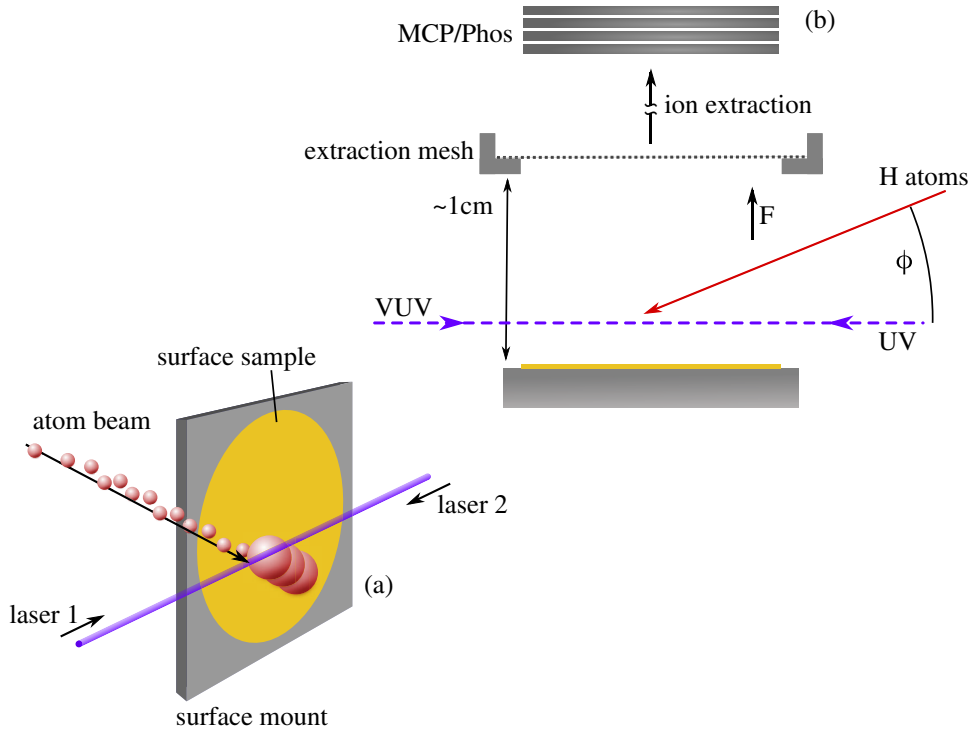

Fig. 9. Experimental apparatus as described in the text. (a) Counter propagating laser beams for Rydberg excitation (parallel to the surface) intersect a beam of hydrogen from supersonic expansion in front of the surface at a distance of ∼2–3 mm. The atom beam is directed towards the surface at an angle of $\phi = 20°$ (the beam valve at a distance of 50 cm is not shown in the drawing). (b) The surface can be potential biased for selection of a particular Stark state in an electric field, F in the interaction region. A mesh grid electrode sits parallel to the surface mount for ion extraction towards a multichannel plate/phosphor-screen detector (the full electrode stack used for ion extraction is not not shown for clarity).

in Fig. 10. Both onset and cutoff of surface ionisation shift towards higher fields when going from the maximum red-shifted ($-k_{\max}$) to the maximum blue-shifted state ($+k_{\max}$). The shift of the field-ionisation signal (high-field cutoff) follows the expected diabatic behaviour as demonstrated previously and illustrated in Fig. 2, but more interestingly, this behaviour also manifests itself for the surface signal.

With respect to the position at which the ion core is formed it would be expected that a red, surface oriented, state ionises furthest from the surface and can be detected at lower fields and a blue, vacuum oriented, state ionises closest to the surface and is detected by higher fields. This expectation is based on the assumption that the approaching atom does not undergo avoided crossings leading to a change in polarisation which was confirmed theoretically in earlier studies [35,69,70]. This is precisely what can be recognised in the surface ionisation profiles in Fig. 10 and, contrary to xenon or the hydrogen molecule, it can be concluded that hydrogen atoms diabatically pass through level crossings as the distance between atom and surface is decreased such that the Stark polarisation is maintained from excitation to the event of ionisation.

When considering only the most red-shifted states, the low-field onset of surface ionisation can be modelled as critical field $F_{\min}$ for ion extraction with Eq. (11) as

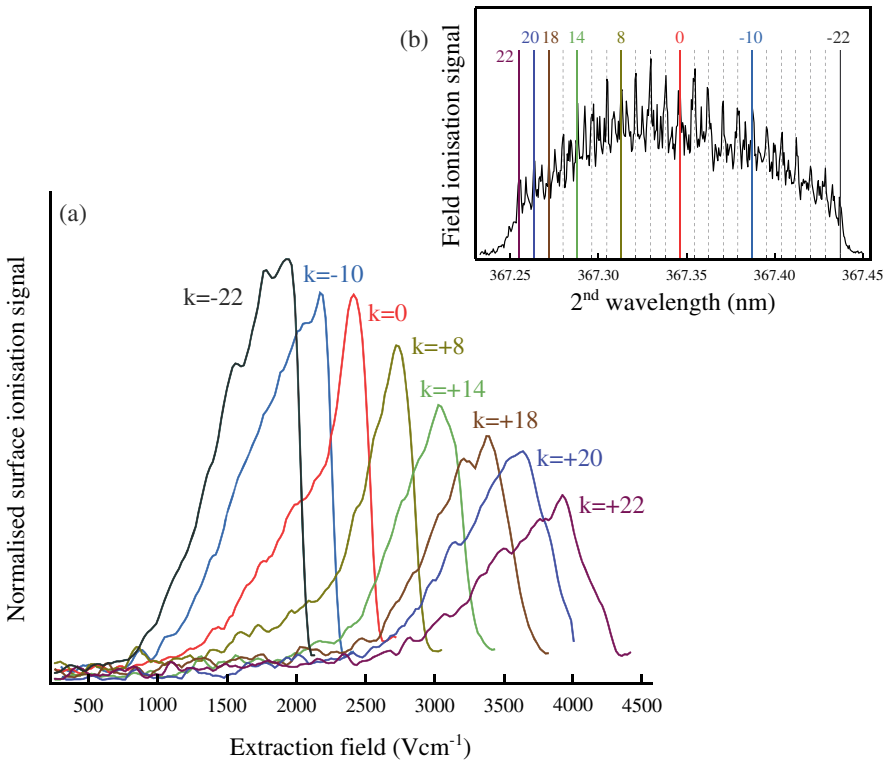

Fig. 10. Surface ionisation profiles for H atoms in $n = 23$ and a range of Stark states are shown in (a). The Stark spectrum obtained by scanning the second laser for excitation from the *2p* state is shown in (b), from which selected states are populated by wavelength selection in a homogeneous field. The surface traces are normalised to the magnitude of the same state during field ionisation. The figure is adapted with permission from reference [31], copyrighted by the American Physical Society.

a critical distance $D_{\min}$ from the OTB approach. When the velocity distribution is convoluted with a step function at the critical distance it does not account for the continuous rise in the surface signal. So et al. used a model that empirically accounts for the shift and broadening of ionisation distances by incorporating a mean critical ionisation distance $\mu(F) = D_{\min}(F) - n^2$ and a spread around this mean $\sigma = 2.5n^2$ into the OTB model to derive a cumulative ionisation probability Φ at distance D,

$$\Phi(D, F) = 1 - \frac{1}{2}\left(1 + \mathrm{erf}\left(\frac{D - \mu(F)}{\sqrt{2\sigma^2}}\right)\right). \tag{14}$$

That equation, when again convoluted with an experimental velocity distribution $f(v_\perp)$, gives an ion detection probability P as

$$P(F) = \int_0^\infty f(v_\perp)\Phi(D_{\min}, F)\,\mathrm{d}v_\perp \tag{15}$$

which provides a very good agreement for the experimental traces from $n = 20$ to 36.

Overall, in this experiment it was demonstrated that hydrogen atoms can be successfully employed in the study of surface ionisation which creates the possibility to directly compare theory to experiment. It also demonstrates that a unique control over the charge polarisation of the Rydberg state can be achieved with atomic hydrogen.

5.3 Energy resolved probes – surface ionisation at electronically structured Cu(100)

The focus of the previous work with atomic hydrogen at a Au sample was how varying the properties of the Rydberg state itself affected the surface ionisation dynamics. The energies of the conduction band in gold are continuous, so any energy of a Rydberg state will be degenerate with a state in the metal that can act as an acceptor for charge transfer. When an electronically structured surface is introduced it is conceivable that surface ionisation via charge transfer is enhanced at discrete resonances.

A Cu(100) surface has a band gap at the energy of the Rydberg states, in which a series of so called image states is set. They arise from the image charge interaction of an electron outside the metal at distance z_e resulting in a Coulomb like potential $V_{ee} = -1/4z_e$ that forms a series of states that extend far into the vacuum in the direction of the surface normal. The wavefunctions of these states could overlap effectively with the incoming Rydberg state wavefunctions. This image state series, which resembles the Rydberg series but with a different periodicity, is of the form

$$E(n_{\mathrm{img}}) = -\frac{1}{16}\,\frac{1}{2(n_{\mathrm{img}}+a)^2} \tag{16}$$

where n_{img} is the index of the image state and a the quantum defect parameter for a given surface. In the direction parallel to the surface the wavefunctions of surface states are similar to the bulk states that form (non-discrete) energy bands so that only the perpendicular component of the velocity is physically relevant.

With the same apparatus as described here and used in reference [31], Gibbard et al. studied surface ionisation at a Cu(100) surface with hydrogen excited to Rydberg states approximately in the middle of the Stark manifold for a range of principal quantum numbers $n = 25$ to 34. The surface is mounted on a translation stage that can transfer the sample into a separate chamber where the copper sample is treated with an ion gun and annealed by repeated heating cycles to ensure a clean and flat sample before Rydberg measurements are conducted. The surface ionisation traces are normalised to the field ionisation signal and integrated from the minimum extraction field to the high-field cutoff and plotted over the principal quantum numbers in Fig. 11. The integrated signal displays non-monotonicity over the principal quantum number and a strong difference compared to a gold surface which possesses no discrete surface energies. These results were explained in terms of resonant enhancement of the ionisation process when the Rydberg energy matches one of the image states of the surface, and therefore illustrates the ability of such studies to probe the electronic structure of surfaces.

Additionally, as described above, the velocity is adjusted to repeat the measurements at a range of collisional velocities, which introduces another handle on probing resonant charge transfer. First, the collisional velocity will affect the ion detection efficiency; from Eq. (10) it can be seen that at a lower velocity of the ion projectile a lower field F_{min} will be necessary for extraction. This shifts the low-field onset in the surface ionisation traces to lower fields and thereby increases the overall amount of integrated signal. Second, this variation with velocity becomes more pronounced for an increased ionisation distance. With greater distance D in Eq. (10), the $\sqrt{T_\perp/D}$ term will become more dominant and lead to greater shifts in the ionisation onset F_{min} over respectively constant $T_\perp$ and thus velocities. Another effect is that a slower atom will spent more time at a certain distance and thereby be more likely to be ionised further away from the surface, also shifting F_{min} to lower fields. The latter is expected to be more important in the case where a Rydberg state is resonant with an image state [72].

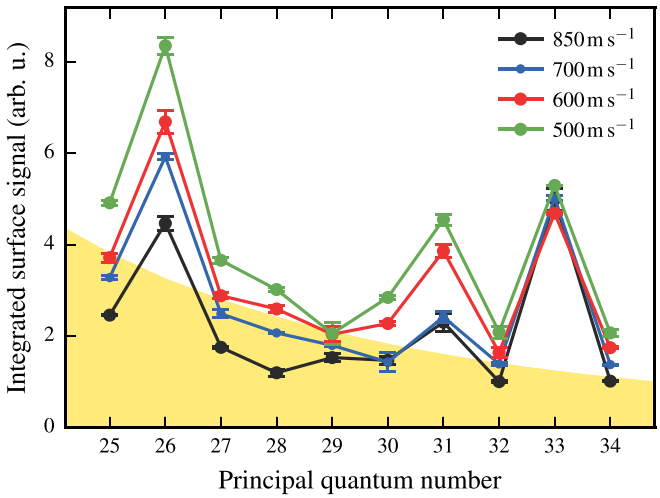

Fig. 11. Integrated surface ionisation profiles for Cu(100) over a range of principal quantum numbers for different collisional velocities, stated is the perpendicular component of the velocity. The yellow background shows the integrated surface ionisation signal for a gold surface at constant velocity, which displays a monotonic behaviour. Figure reproduced from reference [71]. (This figure is subject to copyright protection and is not covered by a Creative Commons license.)

In conclusion, it could be demonstrated that Rydberg atoms display a sensitivity to the discrete electronic structure of a surface by enhanced surface ionisation. The application of this technique can complement previous experimental approaches aimed at the detection of low lying image states [73–75].

6 Future directions

It has been demonstrated that hydrogen Rydberg atoms can be used to energetically probe discrete surface states and by populating different Rydberg states this probe can be adjusted accordingly to the energetics of the system of interest. With the results presented for a Cu(100) surface it becomes intriguing to explore other systems that are of a confined and discrete nature.

Currently, investigations of Rydberg surface ionisation into thin films and nanometre sized particles deposited onto a substrate are being carried out in our group. For thin films it has been shown theoretically that tunneling from atomic levels into a film deposited on an insulating material displays quantum effects and that these are able to strongly influence ionisation rates [76,77]. However, at present the theoretical techniques employed to investigate charge transfer from Rydberg states to a surface are limited to low lying states ($n_{\max} = 10$) which makes it hard to predict the outcome of such measurements. For high lying states the grid sizes of the procedure used in reference [35] become very large ($\propto n^2$) and thereby computationally impractical.

Following the argument from Sect. 5.3, a further decrease in the collisional velocity would increase the time an atom spends at a certain distance from the surface. By spectroscopic means, the uncertainty of a measurement could be decreased by maximising the interaction time with the system in question, e.g. for a discrete energy as the image state of a band gap material.

Figure 12 shows a simulation of the ionisation probability when an excited hydrogen atom approaches a surface for a range of collisional velocities. It illustrates

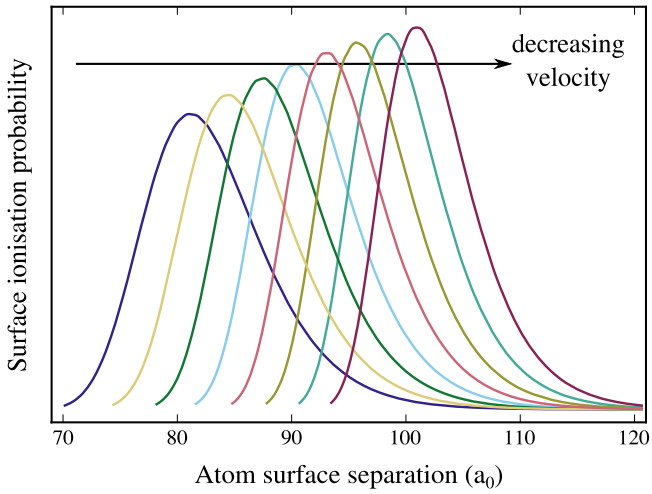

Fig. 12. Simulated surface ionisation probabilities for $n = 5$, $k = -4$, for a range of velocities, calculated with a grid based wavepacket propagation technique as used in [35]. Acceleration of the ion core due to image-charge interaction is not included in the simulation.

how the distance at which surface ionisation occurs is continuously shifted away from the surface as the collisional velocity decreases and also that the spread over which the atom ionises decreases with decreasing velocity by increasing the time the atom spends at a fixed distance. In the current configuration of the apparatus, the velocity selection is limited to what can maximally be achieved with a pulsed valve which, depending on the selected carrier gas that ammonia is seeded with, is approximately 10^2 ms. Presently, we are working on combining the surface experiment with a decelerator based on a chip design [78] that allows a reduction and selection of the collisional velocity after Rydberg excitation before the atoms reach the surface target, paving the way to establish surface ionisation of hydrogen Rydberg atoms as a reliable and more precise tool for surface analysis.

References

1. T.F. Gallagher, *Rydberg Atoms* (Cambridge University Press, Cambridge, UK, 1994)
2. E.A. Hinds, K.S. Lai, M. Schnell, Phil. Trans. R. Soc. Lond. A **355**, 2353 (1997)
3. V. Sandoghdar, C.I. Sukenik, E.A. Hinds, S. Haroche, Phys. Rev. Lett. **68**, 3432 (1992)
4. P. Allmendinger, J. Deiglmayr, J.A. Agner, H. Schmutz, F. Merkt, Phys. Rev. A **90**, 043403 (2014)
5. G. Günter, H. Schempp, M. Robert-de-Saint-Vincent, V. Gavryusev, S. Helmrich, C.S. Hofmann, S. Whitlock, M. Weidemüller, Science **342**, 954 (2013)
6. T. Peyronel, O. Firstenberg, Q. Liang, S. Hofferberth, A.V. Gorshkov, T. Pohl, M.D. Lukin, V. Vuletić, Nature **488**, 57 (2012)
7. O. Firstenberg, T. Peyronel, Q. Liang, A.V. Gorshkov, M.D. Lukin, V. Vuletić, Nature **502**, 7469 (2013)
8. H. Kübler, J.P. Shaffer, T. Baluktsian, R. Löw, T. Pfau, Nat. Photon. **4**, 112 (2010)
9. D. Jaksch, J.I. Cirac, P. Zoller, S.L. Rolston, R.Côté, M. D. Lukin, Phys. Rev. Lett. **85**, 2208 (2000)
10. E. Urban, T.a. Johnson, T. Henage, L. Isenhower, D.D. Yavuz, T.G. Walker, M. Saffman, Nat. Phys. **5**, 110 (2009)
11. M. Saffman, T.G. Walker, K. Mølmer, Rev. Mod. Phys. **82**, 2313 (2010)

12. A. Gaëtan, Y. Miroshnychenko, T. Wilk, A. Chotia, M. Viteau, D. Comparat, P. Pillet, A. Browaeys, P. Grangier, Nat. Phys. **5**, 115 (2009)
13. S.D. Hogan, J.A. Agner, F. Merkt, T. Thiele, S. Filipp, A. Wallraff, Phys. Rev. Lett. **108**, 063004 (2012)
14. A. Wallraff, D.I. Schuster, A. Blais, L. Frunzio, R.-S. Huang, J. Majer, S. Kumar, S.M. Girvin, R.J. Schoelkopf, Nature **431**, 162 (2004)
15. C.E. Theodosiou, Phys. Rev. A **30**, 2881 (1984)
16. W.A. Chupka, J. Chem. Phys. **98**, 4520 (1993)
17. R. Barends, J. Kelly, A. Megrant, D. Sank, E. Jeffrey, Y. Chen, Y. Yin, B. Chiaro, J. Mutus, C. Neill, P. O'Malley, P. Roushan, J. Wenner, T.C. White, A.N. Cleland, J.M. Martinis, Phys. Rev. Lett. **111**, 080502 (2013)
18. A. Tauschinsky, R.M.T. Thijssen, S. Whitlock, H.B. van Linden van den Heuvell, R.J.C. Spreeuw, Phys. Rev. A **81**, 063411 (2010)
19. J.M. Obrecht, R.J. Wild, E.A. Cornell, Phys. Rev. A **75**, 062903 (2007)
20. R. Gerritsma, S. Whitlock, T. Fernholz, H. Schlatter, J.A. Luigjes, J.-U. Thiele, J.B. Goedkoop, Spreeuw, R.J.C., Phys. Rev. A **76**, 033408 (2007)
21. H. Hattermann, M. Mack, F. Karlewski, F. Jessen, D. Cano, J. Fortágh, Phys. Rev. A **86**, 022511 (2012)
22. J. Reichel, V. Vuletic, *Atom Chips* (Wiley-VCH Verlag GmbH & Co. KGaA, Weinheim, Germany, 2011)
23. A. Osterwalder, F. Merkt, Phys. Rev. Lett. **82**, 1831 (1999)
24. J.E. Lennard-Jones, Trans. Faraday Soc. **28**, 333 (1932)
25. N.A. Nguyen, B.K. Dey, M. Shapiro, P. Brumer, J. Phys. Chem. A **108**, 7878 (2004)
26. T.P. Softley, Int. Rev. Phys. Chem. **23**, 1 (2004)
27. C. Fabre, M. Gross, J.M. Raimond, S. Haroche, J. Phys. B **16**, L671 (1983)
28. D.F. Gray, Z. Zheng, K.A. Smith, F.B. Dunning, Phys. Rev. A **38**, 1601 (1988)
29. G.R. Lloyd, S.R. Procter, T.P. Softley, Phys. Rev. Lett. **95**, 133202 (2005)
30. S.B. Hill, C.B. Haich, Z. Zhou, P. Nordlander, F.B. Dunning, Phys. Rev. Lett. **85**, 544 (2000)
31. E. So, M. Dethlefsen, M. Ford, T.P. Softley, Phys. Rev. Lett. **107**, 093201 (2011)
32. A.K. Kazansky, A.G. Borisov, J.P. Gauyacq, Nucl. Instrum. Methods Phys. Res. B **157**, 21 (1999)
33. F.B. Dunning, H.R. Dunham, C. Oubre, P. Nordlander, Nucl. Instrum. Methods Phys. Res. B **203**, 69 (2003)
34. J. Sjakste, A.G. Borisov, J.P. Gauyacq, Phys. Rev. A **73**, 042903 (2006)
35. E. So, M.T. Bell, T.P. Softley, Phys. Rev. A **79**, 012901 (2009)
36. J.M. Wylie, J.E. Sipe, Phys. Rev. A **32**, 2030 (1985)
37. G. Barton, Proc. R. Soc. Lond. A **453**, 2461 (1997)
38. R.P. Abel, C. Carr, U. Krohn, C.S. Adams, Phys. Rev. A **84**, 023408 (2011)
39. J.D. Carter, O. Cherry, J.D.D. Martin, Phys. Rev. A **86**, 053401 (2012)
40. J.D. Bekenstein, J.B. Krieger, Phys. Rev. **188**, 130 (1969)
41. D. Townsend, A.L. Goodgame, S.R. Procter, S.R. Mackenzie, T.P. Softley, J. Phys. B **34**, 439 (2001)
42. E. Vliegen, F. Merkt, Phys. Rev. Lett. **97**, 033002 (2006)
43. Ch. Seiler, S.D. Hogan, H. Schmutz, J.A. Agner, F. Merkt, Phys. Rev. Lett. **106**, 073003 (2011)
44. H.A. Bethe, E.E. Salpeter, *Quantum Mechanics of One- and Two-Electron Atoms* (Springer-Verlag OHG, Germany, 1957)
45. R.J. Damburg, V.V. Kolosov, J. Phys. B **12**, 2637 (1979)
46. K. Ganesan, K.T. Taylor, J. Phys. B **29**, 1293 (1996)
47. Y. Alhassid, E.A. Hinds, D. Meschede, Phys. Rev. Lett. **59**, 1545 (1987)
48. R.O. Jones, P.J. Jennings, O.P. Jepsen, Phys. Rev. B **29**, 6474 (1984)
49. P.J. Jennings, R.O. Jones, M. Weinert, Phys. Rev. B **37**, 6113 (1988)
50. M. Iñarrea, V. Lanchares, J. Palacián, A. Pascual, J. Salas, P. Yanguas, Phys. Rev. A **76**, 052903 (2007)

51. J. Burgdörfer, P. Lerner, F. Meyer, Phys. Rev. A **44**, 5674 (1991)
52. C.A. Kocher, C.R. Taylor, Phys. Lett. A **124**, 68 (1987)
53. H.R. Dunham, S. Wethekam, J.C. Lancaster, F.B. Dunning, Nucl. Inst. Meth. B **256**, 46 (2007)
54. G. Sashikesh, M.S. Ford, T.P. Softley, J. Chem. Phys. **138**, 114308 (2013)
55. G. Sashikesh, E. So, M.S. Ford, T.P. Softley, Mol. Phys. **112**, 2495 (2014)
56. G.E. McCown, C.R. Taylor, C.A. Kocher, Phys. Rev. A **38**, 3918 (1988)
57. M.A. Cazalilla, N. Lorente, R.D. Muino, J.P. Gauyacq, D. Teillet-Billy, P.M. Echenique, Phys. Rev. B, **58**, 13991(1998)
58. E.A. McCormack, E. So, M. Dethlefsen, M.S. Ford, T.P. Softley, J. Phys. B **45**, 015204 (2012)
59. J.C.C. Geerlings, L.F. Tz. Kwakman, J. Los, Surf. Sci. **184**, 305 (1987)
60. S. Wethekam, H.R. Dunham, J.C. Lancaster, F.B. Dunning, Phys. Rev. A **73**, 032903 (2006)
61. D.D. Neufeld, H.R. Dunham, S. Wethekam, J.C. Lancaster, F.B. Dunning, Phys. Rev. B **78**, 115423 (2008)
62. Y. Pu, D.D. Neufeld, F.B. Dunning, Phys. Rev. A **81**, 042904 (2010)
63. P. Nordlander, F.B. Dunning, Phys. Rev. B **53**, 8083 (2006)
64. Y. Pu, F.B. Dunning, Phys. Rev. A **88**, 012901 (2013)
65. G.R. Lloyd, S.R. Procter, E.A. McCormack, T.P. Softley, J. Chem. Phys. **126**, 184702 (2007)
66. E.A. McCormack, M.S. Ford, T.P. Softley, J. Phys. Chem. A **114**, 11175 (2010)
67. S.Y.T. van de Meerakker, H.L. Bethlem, G. Meijer, Nat. Phys. **4**, 595 (2008)
68. S. Willitsch, J.M. Dyke, F. Merkt, Helv. Chim. Acta **86**, 1152 (2003)
69. J. Hanssen, C.F. Martin, P. Nordlander, Surf. Sci. **423**, L271 (1999)
70. N.N. Nedeljković, D.K. Božanić, Phys. Rev. A **81**, 032902 (2010)
71. J.A. Gibbard, M. Dethlefsen, M. Kohlhoff, C.J. Rennick, E. So, M. Ford, T.P. Softley, Phys. Rev. Lett. **115**, 093201 (2015)
72. E. So, J.A. Gibbard, T.P. Softley, J. Phys. B **48**, 175205 (2015)
73. D. Straub, F.J. Himpsel, Phys. Rev. B **33**, 2256 (1986)
74. U. Höfer, I.L. Shumay, Ch. Reu, U. Thomann, W. Wallauer, Th. Fauster, Science **277**, 1480 (1997)
75. P. Wahl, M.A. Schneider, L. Diekhöner, R. Vogelgesang, K. Kern, Phys. Rev. Lett. **91**, 106802 (2003)
76. B. Bahrim, P. Kürpick, U. Thumm, U. Wille, Nucl. Instr. Meth. B **164–165**, 614 (2000)
77. U. Thumm, P. Kürpick, U. Wille, Phys. Rev. B **61**, 3067 (2000)
78. S.D. Hogan, P. Allmendinger, H. Saßmannshausen, H. Schmutz, F. Merkt, Phys. Rev. Lett. **108**, 063008 (2012)